Icarus 309 (2018) 207–219

Contents lists available at ScienceDirect

Icarus

journal homepage: www.elsevier.com/locate/icarus

Implications of the observed Pluto–Charon density contrast

C.J. Bierson[a,*], F. Nimmo[a], W.B. McKinnon[b]

[a] Department of Earth and Planetary Sciences, UC, Santa Cruz, Santa Cruz, CA 95064, USA
[b] Department of Earth and Planetary Sciences and McDonnell Center for the Space Sciences, Washington University in St. Louis, Saint Louis, MO 63130, USA

ARTICLE INFO

Article history:
Received 20 April 2017
Revised 4 October 2017
Accepted 8 March 2018
Available online 15 March 2018

Keywords:
Pluto
Charon
Interiors
Thermal histories

ABSTRACT

Observations by the New Horizons spacecraft have determined that Pluto has a larger bulk density than Charon by 153 ± 44 kg m^{-3} (2σ uncertainty). We use a thermal model of Pluto and Charon to determine if this density contrast could be due to porosity variations alone, with Pluto and Charon having the same bulk composition. We find that Charon can preserve a larger porous ice layer than Pluto due to its lower gravity and lower heat flux but that the density contrast can only be explained if the initial ice porosity is $\gtrsim 30\%$, extends to $\gtrsim 100$ km depth and Pluto retains a subsurface ocean today. We also find that other processes such as a modern ocean on Pluto, self-compression, water-rock interactions, and volatile (e.g., CO) loss cannot, even in combination, explain this difference in density. Although an initially high porosity cannot be completely ruled out, we conclude that it is more probable that Pluto and Charon have different bulk compositions. This difference could arise either from forming Charon via a giant impact, or via preferential loss of H_2O on Pluto due to heating during rapid accretion.

1. Introduction

The New Horizons spacecraft has provided a wealth of new information about the Pluto system (Stern et al., 2015) and has spurred a number of modeling efforts to understand these observations. Desch (2015) and Desch and Neveu (2016) have modeled the process of differentiation on early Pluto and Charon (or their precursors in the case of an impact formation). Malamud et al. (2016) modeled the role serpentinization may play in the extensional tectonics observed on Charon (Beyer et al., 2016). Hammond et al. (2016) used thermal modeling to show that if Pluto's subsurface ocean froze completely ice II may have formed, causing contraction. Given that no contractional features are observed on Pluto's surface they infer that Pluto must still have a subsurface ocean today. In this work we apply a thermal model similar to these to examine the implications of the bulk density difference between Pluto and Charon.

Bulk density is one of the most important measurements for determining the first order structure and composition of any world. Prior to 2015, bulk density measurements of Pluto and Charon were limited by the poorly known radius of Pluto (Tholen and Buie, 1997; Lellouch et al., 2009). This uncertainly was large enough that it could barely be determined whether Pluto and Charon had any difference in density at the 2σ level (Brozović et al., 2015). With the images acquired by New Horizons, the radius of Pluto has been measured with an error of less than two kilometers (Stern et al., 2015; Nimmo et al., 2016). These results show that Pluto and Charon have distinct bulk densities (1854 ± 11 and 1701 ± 33 kg m^{-3} respectively). This difference in density raises the question of whether Pluto and Charon must be compositionally distinct, or if this observation could be consistent with bodies that have the same bulk composition.

This observed difference in density ($\Delta\rho_{PC} = 153 \pm 44$ kg m^{-3}) at first glance appears small given that it is $\sim 10\%$ of Pluto and Charon's bulk density. The changes needed to achieve this density contrast without a difference in bulk composition, however, are dramatic. To give some sense of the scale of change required, it would require melting Pluto's entire ice shell to match the observed density contrast (McKinnon et al., 2017).

Determining if Pluto and Charon have different rock/ice ratios is an important constraint on formation models of the Pluto-Charon system (Nesvorný et al., 2010; Canup, 2005; 2011). There are two primary models for how Pluto and Charon might have formed. One is that Pluto and Charon may have formed in-situ via gravitational collapse (Nesvorný et al., 2010). In this scenario there is no obvious mechanism which might cause one body to preferentially accrete rock or ice; it therefore predicts that Pluto and Charon should have the same initial bulk composition. Alternatively, Charon could have been formed in a giant impact, analogous to the Earth-Moon forming impact. Published models support a low velocity impact between partially differentiated impactors (Canup, 2011). In this sce-

* Corresponding author.
E-mail address: cthomas1@ucsc.edu (C.J. Bierson).

https://doi.org/10.1016/j.icarus.2018.03.007
0019-1035/

Table 1
Parameters used.

	Symbol	Nominal value	Units	Variation range
Reference Viscosity	η_0	10^{14}	Pa s	$10^{13}-10^{17}$
Viscosity Reference Temperature	T_0	270	K	
Activation Energy	Q	60	kJ/mol	
Ice Thermal Conductivity	k_{ice}	$0.4685+488.12/T$	W/(m K)	
Core Thermal Conductivity	k_c	3.0	W/(m K)	$1.0-4.0$
Initial Porosity	ϕ_0	0.2		0.0-0.3
Empirical porosity-conductivity coeff.	a	4.1		
Empirical porosity-conductivity coeff.	b	0.22		
Empirical porosity-conductivity coeff.	ϕ_p	0.7		
Surface Temperature	T_s	40.0	K	
Initial Temperature	T_0	150.0	K	150–250
Ice Specific Heat	Cp_{ice}	1930	J/(kg K)	
Core Specific Heat	Cp_c	1053	J/(kg K)	
Ice Density	ρ_{ice}	950	kg/m^3	950
Ocean Density	ρ_w	1000	kg/m^3	
Core Density	ρ_c	3500	kg/m^3	2500–3500
Latent Heat of Ice	L_H	3.33×10^5	J/kg	

nario there is a grazing impact where a remnant of the impactor is captured (Charon) and a disk of ice-dominated material is created. Some of this disk reaccretes onto Charon and some of the disk may go on to form the smaller outer moons (Canup, 2011), resulting in a Charon that may be ice-rich relative to Pluto.

In this work, we investigate whether the observed bulk density difference *requires* a difference in composition. We examine a number of sources of density contrast to determine if any of those could explain the magnitude of difference observed. We consider density contrasts due to differences in porosity, subsurface oceans, self-compression, water-rock interactions (i.e. serpentinization), and volatile loss. We focus on porosity as it is the mechanism capable of producing the largest density contrast. We find that to match the observed density contrast Charon must have an ice shell with $\sim30\%$ porosity to ~100 km depth. We also present arguments why this large porous layer is unlikely to exist and instead favor a compositional difference between Pluto and Charon to explain the density contrast.

2. Thermal evolution and pore closure model

To test if the density contrast between Pluto and Charon can be explained by differences in the thickness of a porous layer we used a 1D conductive thermal model based on Nimmo and Spencer (2014). We set the same initial rock to ice ratio for Pluto and Charon and model their thermal evolution in order to determine if the density contrast can be explained without differences in composition. The key effects that generate density contrast are changes in the porous structure and the final state of a subsurface ocean.

To fully test porosity as an explanation for the observed density contrast we focus on the most favorable initial conditions. In our model Pluto and Charon are differentiated; this is consistent with the observation that both Pluto and Charon show no compressional features that would be expected from high-pressure ice phases forming at depth if they were not differentiated (Stern et al., 2015; Moore et al., 2016; McKinnon et al., 2017). The initial porosity extends from the surface to the base of the ice shell and has a constant value ψ_0. Having such a thick initial porous layer after differentiation, even if full differentiation follows a giant impact, may or may not be likely but provides an important end-member case. Although we do not explicitly include impact-generation of porosity at later epochs (Milbury et al., 2015), the depth to which such porosity extends will probably be limited to ~10 km at most because of the low velocity and restricted sizes of likely impactors (discussed in Section 4.1). Porosity of the silicate core is unlikely to affect the overall bulk density for reasons discussed in Section 3.2 below.

The start time for thermal evolution is after the decay of short-lived isotopes like ^{26}Al (Kenyon, 2002). Our model takes into account the decay of the long-lived isotopes ^{238}U, ^{235}U and ^{40}K. The abundances of these elements in the core is assumed to be the chondritic value using the abundances of Robuchon and Nimmo (2011). We adopt a cold (150 K), isothermal initial state and assume that a specified porosity initially extends throughout the entire ice mantle. Differentiation probably requires temperatures higher than 150 K, but higher initial temperatures would permit ice flow and reduce the initial porosity. The initial temperature assumed is not very important for the long-term porosity evolution, because the long-term evolution is determined mainly by the energy associated with radioactive decay (Robuchon and Nimmo, 2011). Sensitivity tests found that lowering the initial temperature from 150 K to 50 K lowered the final density of Charon by ~15 kg/m^3 because slightly more porosity was preserved.

We assume both Pluto and Charon have conductive ice mantles (the effect of ice convection is discussed in Section 2.1.2). The local melt temperature of each layer is pressure-dependent following Leliwa-Kopystyński et al. (2002). For all the runs presented here we assume there is no ammonia present (discussed in Section 2.1). We modify the original code of Nimmo and Spencer (2014) to include the variable thermal conductivity of water ice (Petrenko and Whitworth, 2002; Hobbs, 1974; Hammond et al., 2016), the effect of porosity on thermal conductivity, as well as conservation of mass (Appendix A). The model self-consistently adjusts the thermal conductivity (k) for each grid point (i) as pore closure proceeds. We modify the conductivity according to the lower bound derived by Shoshany et al. (2002),

$$k_i(\phi) = k_{ice}(T)\left(1-\frac{\phi}{\phi_p}\right)^{(a\phi+b)} \tag{1}$$

where ϕ is the layer porosity and T is the temperature in Kelvin. $k_{ice}(T)$ and the constants a, b, and ϕ_p are given in Table 1. The effect of porosity on thermal conductivity is generally less than that of the temperature but does become important for high porosity cases ($>20\%$). The temperature dependence of specific heat (Cp) was not included as sensitivity tests found its effect on the long term evolution negligible (less than 0.1% change in the final density for a factor of four change in Cp).

To account for the radial variation in conductivity, layer thickness (Δz), and density (ρ) of each grid point (subscript i), we update the discretized heat conduction equation from Nimmo and Spencer (2014) to use to that of Kieffer (2013) modified to the spherical geometry. The following equation is derived in

Appendix A.

$$\Delta T_i = \frac{-2\Delta t}{\rho_i C p_i \Delta z_i r_i^2}\left[r_{i+1/2}^2 \frac{T_{i+1}-T_i}{\frac{\Delta z_{i+1}}{k_{i+1}}+\frac{\Delta z_i}{k_i}} - r_{i-1/2}^2 \frac{T_i - T_{i-1}}{\frac{\Delta z_{i-1}}{k_{i-1}}+\frac{\Delta z_i}{k_i}}\right]. \tag{2}$$

Here Δt is the model timestep and r_i is the radial location of the cell i.

The change in ϕ with time is modeled as depending on the pressure (P) and viscosity (η) (Fowler, 1985; Nimmo et al., 2003; Besserer et al., 2013) via

$$\frac{d\phi}{dt} = -\phi\frac{P(r)}{\eta(T)}. \tag{3}$$

Besserer et al. (2013) performed a direct comparison of this model with the more sophisticated model of Eluszkiewicz (2004) and qualitative comparisons with Castillo-Rogez et al. (2007) and Eluszkiewicz (1990). In each case they found a negligible difference. The pressure at each radial layer of index i is calculated as

$$P_i = P_{i+1} + \rho_i g_i \Delta z_i \tag{4}$$

where Δz_i and g_i are the layer thickness and the local gravitational acceleration respectively. We assume the surface pressure is $P = 0$. For each layer g_i is computed as

$$g_i = \frac{G}{r_i^2}\sum_{j=0}^{i} m_j \tag{5}$$

where G is the universal gravitational constant and m_j is the mass in layer j. The local viscosity is a strong function of the local temperature (T) and is computed via

$$\eta = \eta_0 \exp\left[\frac{Q}{R_g}\left(\frac{1}{T}-\frac{1}{T_0}\right)\right] \tag{6}$$

where η_0 is the reference viscosity, T_0 is the reference temperature, Q is the activation energy, and R_g is the gas constant.

As pore space closes and an ocean melts/freezes the density, and therefore the thickness, of each layer can change. Because we are interested in the bulk density evolution it is important to conserve mass as these density changes occur. The change in a given layers thickness can be most easily defined in terms of the ratio of the initial to final density of that layer,

$$\Psi \equiv \frac{\rho_0}{\rho_f}. \tag{7}$$

As derived in Appendix A, we can relate Ψ to the change in the radial position of the top of the layer (ΔR) in terms of the initial layer thickness (Δz_0) and the original location of the layer top ($R_{t,0}$) assuming a fixed bottom boundary.

$$\Delta R_t = \left\{\left[\left(1-\frac{\Delta z_0}{R_{t,0}}\right)^3(1-\Psi)+\Psi\right]^{1/3}-1\right\}R_{t,0} \tag{8}$$

After that layer expands or contracts the radial position of all the layers above need to be adjusted accordingly. The spherical geometry causes the change in the radial position of the layer bottom (Δa) to be different from the change of the radial position of the layer top (Δb). For the layer immediately above the layer that has changed density, $\Delta R = \Delta a$. With this constraint, and conservation of volume, we can calculate the change in layer thickness ($\Delta(\Delta z)$) for each layer above the layer that changed density.

$$\Delta b = \left\{\left[\left(1+\frac{\Delta a - \Delta z_0}{R_{t,0}}\right)^3 - \left(1-\frac{\Delta z}{R_{t,0}}\right)^3\right]^{1/3}-1\right\}R_{t,0} \tag{9}$$

$$\Delta(\Delta z) = \Delta b - \Delta a \tag{10}$$

Because the radial position of each layer, R, is assumed to be at the layer center (not the center of mass), the change in the layer center is given as

$$\Delta R = \frac{\Delta a + \Delta b}{2} \tag{11}$$

With the above equations we are able to conserve mass with a relative error over an entire run of $\sim 10^{-5}$. For comparison, runs that keep the layer thickness fixed as the density changes have an error in the mass of $\sim 10^{-2}$.

All of the parameter values used, along with the ranges tested for sensitivity, are listed in Table 1. These parameter values are largely based on those of Robuchon and Nimmo (2011). Each model run uses 100 cells in the core and enough cells in the ice mantle so that the layer thickness is less than 2 km. This spatial scale was determined from a set of resolution tests. The model Δt is recalculated at the start of each timestep using the Courant criterion as

$$\Delta t = 0.3\min(\Delta z_i^2 \rho_i C p_i / k_i). \tag{12}$$

The model is initialized with a constant temperature of 150 K throughout the body and porosity throughout the entire ice shell. Throughout the temperature evolution the surface temperature is fixed at T_s. These initial conditions are set up to be the favorable for porosity surviving in the ice mantle to determine the maximum $\Delta\rho_{PC}$ that can be achieved via a porous ice shell.

2.1. Model results

For each pair of model runs Pluto and Charon are started with their observed mass, a fixed ice to rock ratio, and an initial ice porosity. Because the ice mantle begins porous, the initial radius of Pluto and Charon in most cases exceed their observed values. At the end of each run we can evaluate whether the final radii (and therefore the bulk density) match the observations.

2.1.1. Thermal histories

Before comparing the runs in aggregate it is instructive to look at individual cases. From Eqs. (3) and (6) we can see that both higher pressures (due to large g) and higher temperatures on Pluto should lead to less porosity being preserved through time than on Charon. Each run starts with a silicate interior ($\rho_c = 3500$ kg/m^3) and ice mantle ($\rho_i = 950$ kg/m^3). This ice density is slightly higher than pure water ice ($\sim$920 kg/m^3) to take into account dust and clathrates in the ice shell. The concentration of such impurities is highly uncertain and therefore their potential effects on other parameters such as thermal conductivity are not included in this model. Each of pair of runs starts with a Pluto and Charon that have the same silicate mass fraction (f_{rock}). At the start of each run we introduce an initial porosity, ϕ_0, throughout the ice mantle. This allows us to evaluate the maximum $\Delta\rho_{PC}$ due to differences in the porous structure and the presence of an ocean.

A nominal model output is presented in Fig. 1. On Pluto, the porosity within $\sim$100 km of the core closes on the order of 10^8 years due to the high pressure. Over the first few billion years, the decay of long lived radioisotopes heats the core to $>$1000 K. If the thermal conductivity of the core is high enough and the core is sufficiently dense, an ocean will form that can persist to the present day (See Appendix C). A present day ocean on Pluto is consistent with the model of Hammond et al. (2016) (discussed more below) and some observational evidence (Moore et al., 2016; Nimmo et al., 2016). As this ocean forms and the ice mantle warms, more of the porosity is destroyed by viscous relaxation. The final thickness of the porous layer can vary from 50 to 170 km. The dominant control on this thickness is the initial porosity, ϕ_0, and

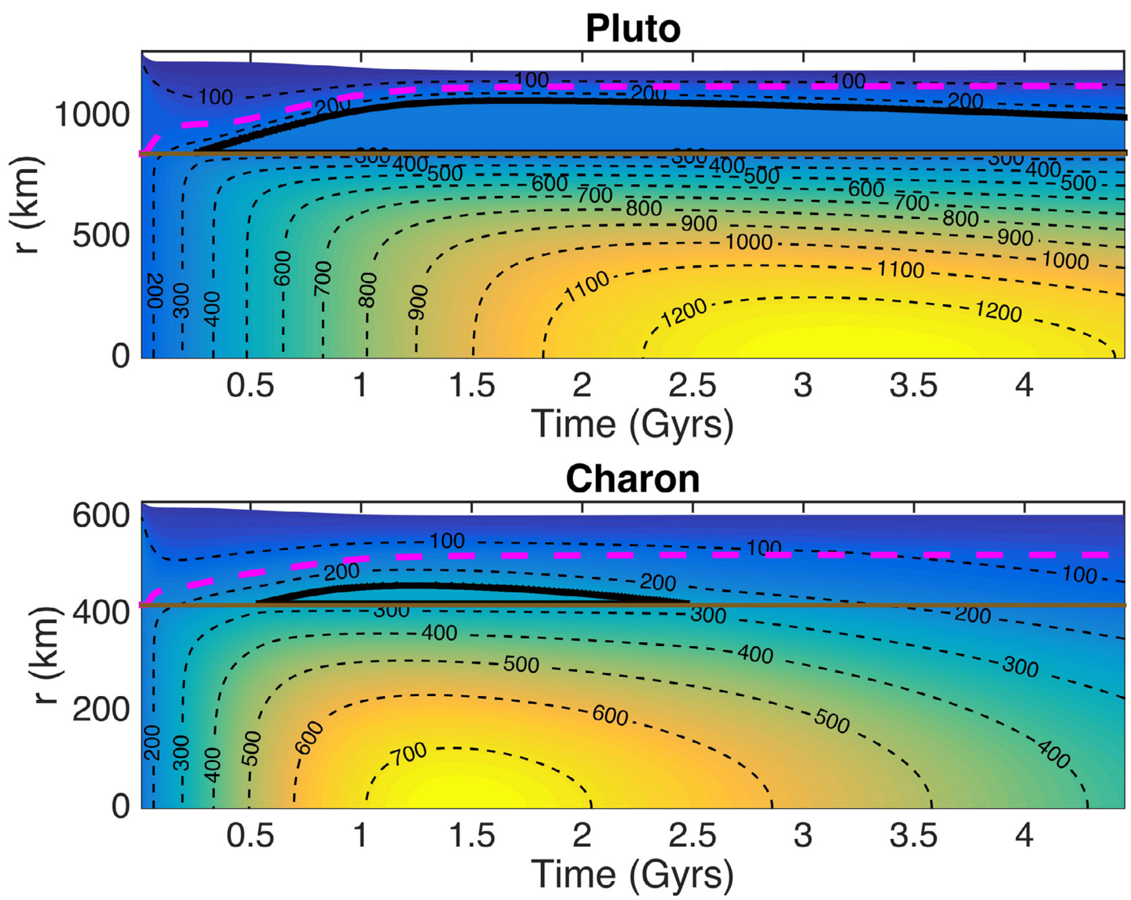

Fig. 1. Thermal histories of Pluto and Charon. For this run $f_{rock} = 0.69$ $\rho_c = 3500$ kg/m^3, $k_{core} = 3.0$ W/ m K, $\phi_0 = 0.30$. Temperature is contoured at a 100 K interval. The horizontal brown line is the top of the silicate core, the dashed magenta line contours the bottom of the porous layer and the thick black line is the top of the ocean layer. In this run Pluto forms a substantial ocean that persists to the present day. Charon forms an ocean 40 km thick that then refreezes. Charon maintains a larger porous layer than Pluto due to lower temperatures and pressure in the ice mantle. At the end of this run Pluto and Charon have radii of 1191 km and 605.2 km. This run gives $\Delta\rho_{PC} = 132$ kg/m^3, within the 1σ error of the observed density contrast.

the thermal conductivity of the core, k_c. If ϕ_0 is larger, the conductivity of the ice shell is reduced by a larger amount (Eq. (1)) causing more heat to become trapped in the ice shell. This raises temperatures, lowering the ice viscosity and destroying more of the porosity. Similarly if k_c is larger heat is more rapidly transferred from the core into the ice and more porosity is destroyed.

On Charon, the final porous layer is generally ~15 km thicker than on Pluto due to Charon's lower gravity and heat flux. For most of the explored parameter space no ocean ever forms on Charon. In those runs when an ocean does form it never persists to the present day (See Appendix C). Not forming an ocean is seemingly at odds with the widespread extensional features on Charon's surface (Moore et al., 2016), but may be reconciled in number of ways. The first is Charon may have had additional heating from tidal dissipation early in its history (Cheng et al., 2014; Barr and Collins, 2015) which would reduce porosity in Charon's shell. Second, Charon may have an ammonia concentration sufficient to allow a cold ocean to form. Such an ocean would not have a significant effect on the preservation of porosity in the upper ice mantle since there would still be a very low heat flux. Third, the extensional features may not be due to the refreezing of an ancient ocean but due to the serpentinization of Charon's silicate core. This is the scenario proposed by Malamud et al. (2016) and discussed further in Section 3.4.

2.1.2. Density contrast results

The results of this parameter space exploration are summarized in Fig. 2. The largest control on the bulk density is the initial porosity. In particular, to generate the observed $\Delta\rho_{PC}$, an initial porosity of 30% or more is required for almost all parameter combinations. This high porosity needs to extend to significant depths ($\gtrsim$100 km) but this is easily achieved due to the low temperatures and pressure in Charon's ice shell. Charon could still develop an ocean < 50 km thick which then refroze (consistent with the observed extensional tectonics; (Beyer et al., 2016)) without violating this depth requirement. We widely varied the ice viscosity, initial porosity, core conductivity, melting temperature, and core density to characterize the sensitivity of our results (Table 1). Changes in η_0 and k_c have a notable effect on how much porosity is preserved, but have a small effect on $\Delta\rho_{PC}$ because the magnitude of this change is nearly equal on Pluto and Charon. Changing the core density does change f_{rock} but because the effect is the same on Pluto and Charon it does not generate a density contrast.

It is important to investigate how the presence of ammonia would affect our results. If the oceans of Pluto and Charon contain a significant fraction of ammonia they will be colder, larger in extent, and less dense. The colder ocean will limit the heat flux in the ice shell causing porosity to only be destroyed nearer the ocean itself and potentially only when the ice melts. This effect however, will be outweighed by the fact that a larger ocean will form. Of importance for this work, there is no reason to suspect radically different ammonia concentrations on Pluto and Charon and as such

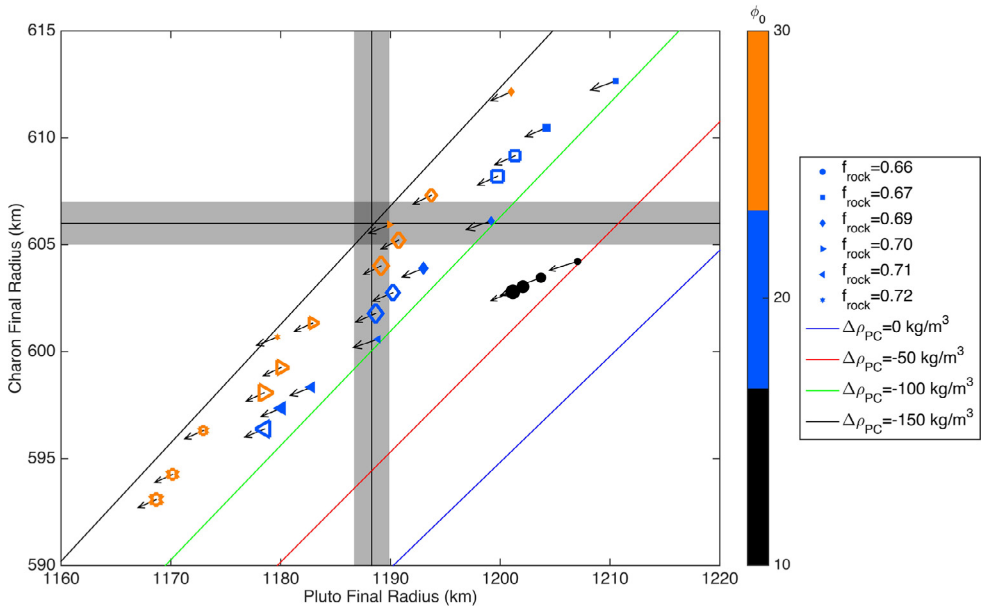

Fig. 2. Final radius for all model runs with $\rho_c = 3500$ kg/m^3, $\rho_{ice} = 950$ kg/m^3, $\eta_0 = 10^{14}$ Pa s. In all cases the mass of Pluto and Charon is consistent with the observations. Solid lines are lines of constant density contrast. Symbols indicate different rock mass fractions. This size of the points scales with k_c which was varied from 1.0–4.0 W/(m K) in integer increments. Unfilled markers indicate Charon formed an ocean > 10 km thick (Appendix C). Arrows show the effect that would result from gravitational self-compression (Section 3.1). Note that only porosity has a strong effect $\Delta\rho_{PC}$.

this will have a negligible impact on our results. If there is a significant fraction of ammonia in Pluto's modern ocean it would make that ocean less dense, the opposite effect that would be needed to explain $\Delta\rho_{PC}$. These effects together imply that our results (with no ammonia) may represent the best case scenario for generating a density contrast without requiring bulk compositional variation.

Another factor not in our model is convection in the core and/or ice shell. If the cores of Pluto and Charon are porous, hydrothermal convection could occur for permeability above $\sim 10^{-15}$ m^2 (Turcotte and Schubert, 2014). This would increase the heat flux out of the core. This would have the same effect on the ice shell as varying the thermal conductivity of the core shown in Fig. 2 (more discussion in Section 3.2). Ice shell convection is unlikely to occur on Charon due to its small size. In contrast, Robuchon and Nimmo (2011) found that for Pluto with $\eta_0 < 5 \times 10^{15}$ Pa s convection occurs. Robuchon and Nimmo (2011) find that when present, the more efficient heat transport due to convection cools the ice shell and prevents an ocean from forming. Conductive and convective shells develop near-surface temperature structures which are almost identical (Robuchon and Nimmo, 2011), because irrespective of how heat is transferred at depth, in the near-surface conduction always dominates. Since it is only in this cold region that porosity can persist, the porosity structure will be almost unaffected by whether conduction or convection operates. In contrast, the lack of a thick ocean for a convective Pluto would lead to a less dense Pluto, making the density contrast harder to explain. Again this implies that our model runs are providing an estimate of the maximum density contrast case.

2.1.3. Comparisons to other thermal models

The only other Charon model to estimate pore closure is described in Malamud and Prialnik (2015) and Malamud et al. (2016). The aim of Malamud and Prialnik (2015) was to explain the difference in density between Charon, Orcus, and Salacia as differences in the porosity of these three Kuiper belt objects. Malamud et al. (2016) used an updated version of the same model to understand the extensional features on Charon found by New Horizons (Stern et al., 2015; Moore et al., 2016). There are two important differences between these models and the one presented here. The first is that these models include serpentinization, and as of Malamud et al. (2016), dehydration reactions between the originally anhydrous silicates and water. This does affect the energy balance of the system as serpentinization reactions are exothermic. This difference (and others) means that Malamud et al. (2016) find core temperatures that are ~200 K higher than in our model. If this were to be included in our model the increase in heat flux would reduce the amount of porosity that survives on Pluto and Charon to the present day (reducing the density contrast). Given the large uncertainties involved with modeling these reactions (Section 3.4) we chose not to include them in our model.

The second important difference is in how porosity is treated. The model of Malamud and Prialnik (2015) and Malamud et al. (2016) use an empirical relationship between pressure, temperature, and porosity based on experimental data from Durham et al. (2010) and Yasui and Arakawa (2009). We adopt the physical model presented in Section 2.1.1. The main difference in these methods is that in the parametrization method of Malamud and Prialnik (2015) and Malamud et al. (2016) ice of the same pressure and temperature will apparently always have the same porosity independent of its history (silicate porosity in their model does have a thermal memory and will not reform porosity). With the method used in this study, once porosity is destroyed it is never reformed. It is not clear what physical process may create new porosity at depth where this difference is likely to manifest. We adopt the simple model described by Eq. (3) so we can better interpret the effect parameters like k_c and η_0 have on the porosity evolution.

Another model that includes the effects of serpentinization is that of Desch and Neveu (2016). This model also tracks composition, including ammonia along the eutectic as oceans form. This focus of this model was for understanding the evolution of subsurface oceans on Pluto and Charon and their implications for cryovolcanism on these worlds. Given this aim they do not model porosity in the ice shell. Because of the larger number of additional factors tracked in Desch and Neveu (2016) and a limited set of published thermal histories we were not able to make a direct comparison between their model and the one presented here.

The thermal model used here is very similar to Hammond et al. (2016). Hammond et al. (2016) include the formation of ice II which can, in some circumstances, occur on Pluto if the ocean freezes completely. Because of the lack of observed compression features and noted extensional features on Pluto (Moore et al., 2016), they conclude that Pluto must still have a subsurface ocean and therefore there is no ice II in the ice shell. Given this result we do not include the formation of ice II in our model.

Because of the similarity between our model and Hammond et al. (2016) we tried to benchmark our model against theirs. We found that our model results for the heat flux and ocean thickness through time are very similar to Hammond et al. (2016) for $k_c = 2$ W m^{-1} K^{-1}. However, Hammond et al. (2016) predict Pluto should have a thicker ocean for lower k_c, while we find the opposite effect (See Appendix C). This discrepancy results from a minor error in the code of Hammond et al. (2016); their corrected results now agree with ours (Hammond, pers. comm).

3. Other mechanisms

3.1. Self-compression

One potential mechanism for generating a denser Pluto is the bulk compression of Pluto's interior under the greater lithostatic pressure (P). For environments where the pressure is less than the bulk modulus (K) of the material, as is the case for Pluto and Charon, the change in the material density is given by

$$\frac{d\rho}{\rho} \approx \frac{dP}{K}. \tag{13}$$

Due to the low gravity of Pluto and Charon this is a relatively small change in the bulk density. For these calculations we calculate P as shown in Eq. (4) and nominal values for the bulk modulus of ice ($K_{ice} = 10^{10}$ Pa) and silicates ($K_{rock} = 10^{11}$ Pa). The effect of applying Eq. (13) as a post-processing step to our model runs is shown as arrows in Fig. 2. In general this generates a difference in bulk density between Pluto and Charon of $\Delta\rho \sim 15$ kg/m^3.

3.2. Core porosity

In our model we only include porosity in the ice shell of Pluto and Charon. Porosity likely also exists in their cores but given the warm core temperatures this pore space would likely be filled with liquid water. The question for this study is what effect would changes in the core porosity have for the bulk porosity. When the porosity in the ice mantle closes the ice becomes denser, lowering the bulk volume of the body. Conversely, when the fluid-filled pores in the core close the water is redistributed from the inner parts of the core to the base of the ocean. If that water stays liquid there is no change in the bulk volume, and therefore the bulk density is unaffected. If the water squeezed out of the core then freezes the body radius would increase and thereby lower the bulk density. Because the compressibility of water is much lower than that of rock, as the water migrates upwards it will expand slightly in accordance with Eq. (13).

Due to the low pressures and low temperatures (Eq. (3)) we find for a silicate viscosity following an Arrhenius dependence (Eq. (6), $\eta_0 = 10^{20}$ Pa s, $Q = 300$ kJ/mol, $T_0 = 1400$ K) nearly all porosity present in Charon's core could survive the history of the solar system (in the absence of water-rock reactions, considered below). On Pluto there may be significant pore closure. As noted above however, if the water remains liquid (as would be the case if Pluto has a present day ocean (Hammond et al., 2016; Nimmo et al., 2016; Moore et al., 2016)) Pluto's bulk density would would be slightly lowered, the opposite effect needed to match the observations. If the water from Pluto's core froze it would also lower Pluto's bulk density. If Charon has a more porous core than Pluto it could also have a lower thermal conductivity unless hydrothermal circulation were operating (Malamud et al., 2016). This also does not help to match the observations because in many model runs nearly all the porosity in Charon's ice shell survives. Our ability to match the observations is limited by the amount of porosity that can be removed from Pluto's ice shell. This porosity reduction would be increased if the core conductivity of Pluto were increased, e.g., by hydrothermal circulation. In the absence of such an effect, porosity in the core of Pluto or Charon, or changes in that porosity, are unlikely to have any effect on their bulk density and may only lower the density of Pluto.

3.3. Thermal expansion

Assuming a cold start, as Pluto and Charon warm they will expand. We can estimate how this will affect the bulk density of each object by combining the density change due to a change in volume (ΔV),

$$\frac{-\Delta\rho}{\rho} = \frac{\Delta V}{V} \tag{14}$$

with the volume change due to thermal expansion,

$$\Delta V \approx V\alpha_v \Delta T. \tag{15}$$

Here α_v is the volumetric thermal expansion coefficient. Using $\alpha_{v,ice} \approx 10^{-4}$, $\alpha_{v,rock} \approx 3 \times 10^{-5}$ and the temperature changes observed in our modeling ($\Delta T_{ice} \approx 100$ K, $\Delta T_{rock} \leq 1000$ K) we estimate $\Delta\rho \leq -10$ kg/m^3. Because Pluto will experience higher internal temperatures than Charon, this effect will be larger on Pluto (Pluto will become less dense). This means thermal expansion would produce a small density contrast with the opposite sign to the observed $\Delta\rho_{PC}$.

3.4. Serpentinization

If Pluto and Charon have, or have had, active hydrological systems we would expect water-rock interactions to modify their mineralogy and therefore their density structure. The extent to which this would occur on Pluto and Charon depends on a wide range of poorly constrained parameters including the mineralogy and hydrology of their cores. Modeling by Malamud et al. (2016) suggest that this process could be widespread at least on Charon.

When anhydrous rock and water react to form serpentine the net result is an increase in density. We can determine how much serpentinization would need to occur to explain the observed density contrast to assess its plausibility. Applying Eq. (14), we can relate ΔV to the change in volume due to producing one mole of serpentinite, ΔV_S by also including the number of moles of serpentinite, N_S.

$$\Delta V = N_S \Delta V_S \tag{16}$$

The volume change per mole is calculated by

$$\Delta V_S = \sum_{products} n_i \frac{M_i}{\rho_i} - \sum_{reactants} n_j \frac{M_j}{\rho_j} \tag{17}$$

where n_x is the number of moles of the species involved in the reaction, M_x is the molar mass of the species, and ρ_x is the density of the species. Values of ΔV_S calculated for different serpentine reactions are given in Table 2. Because all these reactions increase the bulk density, Pluto would have to be more serpentinized than Charon to explain the observed density contrast. Associated magnetite-forming reactions (Vance et al., 2016) also increase the bulk density. We can relate the volume of Pluto that would need to

Table 2
Volume change per mole serpentinite produced calculated using Eq. (17). Reaction 1 is that used by Malamud et al. (2016). All reactions result in an overall decrease in volume which would lead to a larger bulk density. Mineral densities used are all at Earth surface temperature and pressure (Table B.3).

	Reaction	ΔV_S (m^3/mol)
1)	$Mg_2SiO_4 + MgSiO_3 + 2H_2O \rightarrow Mg_3Si_2O_5(OH)_4$	$< 10^{-6}$ [a]
2)	$3Mg_2SiO_4 + SiO_2 + 4H_2O \rightarrow 2Mg_3Si_2O_5(OH)_4$	-8.5×10^{-6}
3)	$2Mg_2SiO_4 + 3H_2O \rightarrow Mg_3Si_2O_5(OH)_4 + Mg(OH)_2$	-1.1×10^{-5}

[a] Value is uncertain due to the small differences in mineral density and the precision of the density measurements (Ahrens and Gaffney, 1971).

be occupied by serpentinite, V_S to produce $\Delta\rho_{PC}$, using the density of serpentinite (ρ_S) and the molar mass of serpentinite (M_S).

$$N_S = \frac{V_S \rho_S}{M_S} \tag{18}$$

$$\frac{-\Delta\rho}{\rho} = \frac{N_S \Delta V_S}{V} \tag{19}$$

$$\Rightarrow \frac{V_S}{V} = \frac{-\Delta\rho}{\rho}\frac{M_S}{\Delta V_S \rho_S} \tag{20}$$

Depending on the assumed reaction taking place (Table 2), Eq. (19) predicts ~80% of Pluto's total volume would have to be serpentinized to match the observed density contrast. This estimate is a lower limit as it assumes no serpentinization in Charon.

The volume fraction of Pluto and Charon that undergo serpentinization is dependent on the availability of water in the silicate core and the thermal stability of serpentine minerals. Ideally we could choose a temperature cutoff above which serpentinite is unstable and track that isotherm in the model output. The model of Desch and Neveu (2016) has dehydration occur over a range of temperatures between 700–850 K. Malamud and Prialnik (2016) use temperature-dependent reactions rates from experiments by Sawai et al. (2013) and estimate such a cutoff at 675 K. The experimental data is mixed with prograde experiments (constantly increasing temperature with time) finding dehydration temperatures of 875 K to 1075 K (Sawai et al., 2013) while isothermal studies find dehydration temperatures of 725 K to 875 K (Wegner and Ernst, 1983; Candela et al., 2007; Inoue et al., 2009; Dlugogorski and Balucan, 2014). Because of this large uncertainty we opt to not choose any particular temperature for the stability and instead do a more qualitative comparison between Pluto and Charon. Because Charon has lower core temperatures, a much larger volume fraction of Charon's core will be favorable for serpentinite compared to Pluto. This would have the net effect of making Charon more dense than Pluto, the opposite of the observations. It is hard to contrive a situation wherein Pluto would be more serpentinized than Charon.

Given that Charon is likely to be more serpentinized and serpentinization increases the bulk density, we expect serpentinization to have the opposite net effect to that needed to explain the observed density contrast. It is worth noting that there may be secondary chemical reactions may have moderating effects. In summary, while more detailed modeling could be carried out, the simple analysis used here implies that serpentinization is unlikely to explain the density contrast.

3.5. Volatile loss

Spectroscopic data of Pluto's surface suggests it has more high vapor pressure volatile elements including, N_2, CH_4, and CO, than Charon (Buie et al., 1987; Marcialis et al., 1987; Protopapa et al., 2008; Cruikshank et al., 2015). These findings have been confirmed by New Horizions which found that Charon's surface is almost exclusively water ice with some exposed NH_3 around fresh craters (Grundy et al., 2016). This difference is likely due to Charon's lower gravity allowing these volatiles to be lost to space via escape processes (Schaller and Brown, 2007; Brown, 2012). There are no observations that allow us to determine if Charon has lost its entire inventory of these volatile species or if isome are retained in the subsurface.

For this work it is of interest to determine how the loss of these volatile ices would affect Charon's bulk density. To make an initial estimate we assume cometary abundances of these species relative to water (Eberhardt et al., 1988; Crovisier, 1994; Mumma and Charnley, 2011). We focus on CO as it is an order of magnitude more abundant than N_2 and CH_4 and accordingly has the largest impact on the bulk density change. Assuming a CO ice density of 1000 kg/m^3 (Jiang et al., 1975) and present at 10% abundance relative to water ice, the loss of all CO would lead to an increase in the bulk density of Charon by ~200 kg/m^3. While we do not know what fraction of Charon's volatile ices have been lost, this effect has the opposite sign of what would be needed to explain the Pluto-Charon density contrast.

4. Discussion

The difference in density between Pluto and Charon appears at a first glance to be too small to be of much significance. However, what our analysis shows is that assuming the same bulk composition, this density contrast can only be explained if Charon has a high initial porosity ($\gtrsim$30%), that still extends to great depths in Charon's ice shell ($\gtrsim$100 km) *and* Charon has not lost a significant fraction of its volatile ices (Section 3.5) *and* is not significantly more serpentinized than Pluto (Section 3.4).

4.1. Initial porosity

Forming and retaining a thick ($\gtrsim$100 km) porous layer within Charon is required to explain the observed density contrast. Impacts are known to be able to both create and destroy porosity. Which effect dominates depends on the details of the impact including the preimpact porosity (Arakawa et al., 2002; Milbury et al., 2015). The aggregate long term effect is impacts generate porosity up to some equilibrium value. On the Moon, impact-generated porosity of 15% persists to depths of ~15 km (Wieczorek et al., 2013; Besserer et al., 2014); the lower-velocity impacts in the Pluto-Charon system may result in a thinner impact-generated porous layer. Thus, the thick porous layer required to match the density contrast must be the result of primordial (accretionary) processes. This could include one or more giant impacts. Given the geologic evidence that Charon is differentiated (Stern et al., 2015; Moore et al., 2016; McKinnon et al., 2017), this porous layer must also survive (or be formed after) the differentiation and/or impact formation process.

Unfortunately, there is as yet little understanding of how porosity accumulates during the accretion process. Comets have a porosity of 60% – 90% (Consolmagno et al., 2008), and Hyperion, with a mean radius of 135 km, has a porosity of >40% (Thomas et al., 2007). Larger bodies are expected to retain less porosity due to self-compaction. Baer et al. (2011) show that estimated asteroid porosities decrease with increasing size, with estimated porosities of up to 60% at 150 km radius but not exceeding 20% for bodies with radii in excess of 200 km. This holds for both S and C group main belt asteroids, the only two groups for which enough data was available. Ice has a compressional strength an order of magnitude less than that of rock, and ice flows more readily at the same temperature, so icy bodies of a comparable size would be expected to have less porosity[1] Yasui and Arakawa (2009) use experimental measurements to suggest a maximum porosity of 20% for ice at 218 K and 30 MPa (the pressure at 100 km depth on Charon). Taken together, these results suggest that requiring 30% porosity to extend to > 100 km on depth is unlikely.

4.2. Early hydrodynamic escape

It has previously been assumed that if Pluto and Charon formed via gravitational collapse, they should have the same bulk composition (Nesvorný et al., 2010). We suggest that this may not necessarily be the case if, during formation, Pluto lost more low vapor pressure volatiles (i.e. H_2O) than Charon via atmospheric escape processes. The rate of gravitational energy deposition during accretion is dependent on the mass of the accreting body and the rate of accretion. If the timescale for accretion is short enough, Pluto, but not necessarily Charon, would form a steam atmosphere from which volatiles can escape. To estimate what timescales are needed for this to be the case we can balance the incoming gravitational energy with the outgoing radiative flux,

$$4\pi R^2 \sigma T_{surf}^4 \approx \frac{3}{5}\frac{Gm^2}{R}\frac{1}{\tau} \tag{21}$$

where σ is the Stefan–Boltzmann constant, m is the planet mass, R is the planet radius, and τ is the timescale of formation. This calculation ignores the energy lost to the gas drag which should be negligible (Nesvorný et al., 2010). From this we can make an order of magnitude estimate of the timescale of accretion, τ, needed to bring the surface temperature high enough to have liquid water on the surface. For Pluto's surface to reach 270 K it would need to form in $\tau < 0.1$ Myr, while Charon would have to form in $\tau < 0.01$ Myr. Coagulation models of KBO formation suggest formation timescales of one to tens of millions of years (Kenyon and Luu, 1999; Kenyon et al., 2008; Johansen et al., 2015), however gravitational collapse models favor a formation timescale of order hundreds of years (Nesvorný et al., 2010).

If Pluto's surface temperature does exceed the melting point of water it is still difficult to estimate the mass lost to space. Atmospheric loss from a young Pluto should be dominated by hydrodynamic escape due to Pluto's weak gravity (Trafton, 1980; Hunten and Watson, 1982). Hydrodynamic escape depends strongly on the gas density and temperature structure of the atmosphere (Tian et al., 2005; Tian and Toon, 2005), both of which are almost completely unknown. Models of the Earth's primitive atmosphere suggest that a steam atmosphere developed that limited the heat flux to space (Goldblatt et al., 2013). It is unclear what conditions might lead to a similar steam atmosphere on Pluto, and what would occur if the energy from impactors exceeded the rate at which that steam atmosphere can radiate. Because of the large uncertainties associated with atmospheric loss, we do not think a reasonable estimate can be made for the density contrast that might arise from such a process. Future work is needed to more fully understand volatile loss during rapid formation of medium-sized icy worlds.

4.3. Implications for other KBOs

If Pluto and Charon have different bulk compositions, that helps constrain how they - and potentially other Kuiper Belt objects - formed. These issues are discussed at length in McKinnon et al. (2017), but we will briefly mention some key issues here. Although the different compositions of Pluto and Charon could potentially be reconciled with direct gravitational collapse (see above), the existence of the small icy satellites of Charon does not support this hypothesis. The Pluto-Charon system more likely formed from a giant impact between partially-differentiated precursors (Canup, 2011); similar giant impacts are also likely responsible for the extreme variation in density observed across other, comparably-sized KBOs (McKinnon et al., 2017). Unfortunately, the differentiation state of these bodies is poorly known, but it seems likely that different accretion scenarios will lead to quite different predicted internal structures.

[1] Some asteroids may have undergone compaction due to early ^{26}Al heating. This process is less likely to be relevant in the outer solar system due to much longer formation timescales (Kenyon, 2002).

5. Conclusion

The difference in Pluto and Charon's density can only be explained by porosity alone in a very extreme case (>30% initial porosity). Arguments presented above suggest that such high initial porosity values are unlikely for such large objects. From this we conclude that Pluto and Charon must have different rock to ice ratios with Pluto having a larger silicate fraction. This observation is consistent with an impact formation model of the Pluto–Charon system or a scenario whereby Pluto formed quickly enough to lose a significant fraction of its original water ice content via accretional heating. Future works should investigate the feasibility of forming Pluto fast enough for this mechanism to occur and the amount of volatiles that may escape during this formation period.

Acknowledgments

We would like to thank Uri Malamud for a very helpful discussion on serpentinization in icy worlds and Noah Hammond for helping to perform a model benchmark. We also thank Noah Hammond and an anonymous reviewer for their helpful comments. This material is based upon work supported by the National Science Foundation Graduate Research Fellowship under Grant No. NSF DGE 1339067 and the New Horizons project.

Appendix A. Mass conservation derivations

As a layer changes in density it will change in volume to conserve mass. Using conservation of mass we can solve for the change in radius of the layer that is changing mass. In the following R_t and R_b denote the upper and lower bound of a layer.

$$M_0 = M_f \tag{A.1}$$

$$\rho_0(R_{t,0}^3 - R_{b,0}^3) = \rho_f(R_{t,f}^3 - R_{b,f}^3) \tag{A.2}$$

$$\Psi = \frac{\rho_0}{\rho_f} = \frac{R_{t,f}^3 - R_{b,f}^3}{R_{t,0}^3 - R_{b,0}^3} \tag{A.3}$$

$$\Psi R_{t,0}^3 - \Psi R_{b,0}^3 = R_{t,f}^3 - R_{b,f}^3 \tag{A.4}$$

Let $R_{b,0} = R_{b,f}$ (fixed bottom boundary)

$$R_{t,f}^3 - \Psi R_{t,0}^3 = R_{b,0}^3(1 - \Psi) \tag{A.5}$$

$$\Delta R_t = R_{t,f} - R_{t,0} \tag{A.6}$$

$$(\Delta R_t + R_{t,0})^3 - \Psi R_{t,0}^3 = R_{b,0}^3(1 - \Psi) \tag{A.7}$$

$$\left(1 + \frac{\Delta R_t}{R_{t,0}}\right)^3 - \Psi = \left(\frac{R_{b,0}}{R_{t,0}}\right)^3 (1 - \Psi) \tag{A.8}$$

Let $\Delta z = R_{t,0} - R_{b,0}$

$$\left(1 + \frac{\Delta R_t}{R_{t,0}}\right)^3 = \left(1 - \frac{\Delta z}{R_{t,0}}\right)^3 (1 - \Psi) + \Psi \tag{A.9}$$

$$\Delta R_t = \left\{\left[\left(1 - \frac{\Delta z}{R_{t,0}}\right)^3 (1 - \Psi) + \Psi\right]^{1/3} - 1\right\} R_{t,0} \quad \text{(A.10)}$$

Because of the spherical geometry each layer will change thickness by a different amount. In the following let Δa and Δb be the change in radial position at the locations R_b and R_t respectively. Δa is known from the previous layer so for each layer we must solve for Δb.

$$\Delta a \equiv R_{b,f} - R_{b,0} \quad \text{(A.11)}$$

$$\Delta b \equiv R_{t,f} - R_{t,0} \quad \text{(A.12)}$$

$$\Delta z_0 \equiv R_{t,0} - R_{b,0} \quad \text{(A.13)}$$

$$\Delta(\Delta z) \equiv \Delta z_f - \Delta z_0 = \Delta b - \Delta a \quad \text{(A.14)}$$

$$V_0 = V_f \quad \text{(A.15)}$$

$$R_{t,0}^3 - R_{b,0}^3 = R_{t,f}^3 - R_{b,f}^3 \quad \text{(A.16)}$$

$$R_{t,f}^3 - R_{t,0}^3 = R_{b,f}^3 - R_{b,0}^3 \quad \text{(A.17)}$$

$$(\Delta b + R_{t,0})^3 - R_{t,0}^3 = R_{b,f}^3 - R_{b,0}^3 \quad \text{(A.18)}$$

$$\left(\frac{\Delta b}{R_{t,0}} + 1\right)^3 - 1 = \frac{R_{b,f}^3 - R_{b,0}^3}{R_{t,0}^3} \quad \text{(A.19)}$$

$$\left(\frac{\Delta b}{R_{t,0}} + 1\right)^3 - 1 = \left(\frac{R_{b,f}}{R_{t,0}}\right)^3 - \left(\frac{R_{b,0}}{R_{t,0}}\right)^3 \quad \text{(A.20)}$$

$$\left(\frac{\Delta b}{R_{t,0}} + 1\right)^3 - 1 = \left(\frac{\Delta a - \Delta z_0 + R_{t,0}}{R_{t,0}}\right)^3 - \left(\frac{R_{t,0} - \Delta z_0}{R_{t,0}}\right)^3 \quad \text{(A.21)}$$

$$\left(\frac{\Delta b}{R_{t,0}} + 1\right)^3 - 1 = \left(1 + \frac{\Delta a - \Delta z_0}{R_{t,0}}\right)^3 - \left(1 - \frac{\Delta z_0}{R_{t,0}}\right)^3 \quad \text{(A.22)}$$

$$\Delta b = \left\{\left[\left(1 + \frac{\Delta a - \Delta z_0}{R_{t,0}}\right)^3 - \left(1 - \frac{\Delta z_0}{R_{t,0}}\right)^3\right]^{1/3} - 1\right\} R_{t,0} \quad \text{(A.23)}$$

Appendix B. Mineral densities

Table B1
All values are for surface pressure and temperature. Water was assumed to have a density of 1000 kg/m^3.

Mineral name	Formula	Density (kg/m^3)	Source
Chrysotile	$Mg_3Si_2O_5(OH)_4$	2500	Pundsack (1956)
Forsterite	Mg_2SiO_4	3200	Graham and Barsch (1969)
Enstatite	$MgSiO_3$	3300	Ahrens and Gaffney (1971)
Silica	SiO_2	2300	Irene et al. (1982)
Brucite	$Mg(OH)_2$	2400	Jiang et al. (2006)

Appendix C. Ocean thickness

Given our discrepancy on the dependence of the ocean thickness to core conductivity compared with Hammond et al. (2016) we want to clearly present on results here. Fig. C.3 is an attempt to replicate Hammond et al. (2016) Figure S3 (0% ammonia). It is not clear why our final ocean thickness are about half that calculated by Hammond et al. (2016).

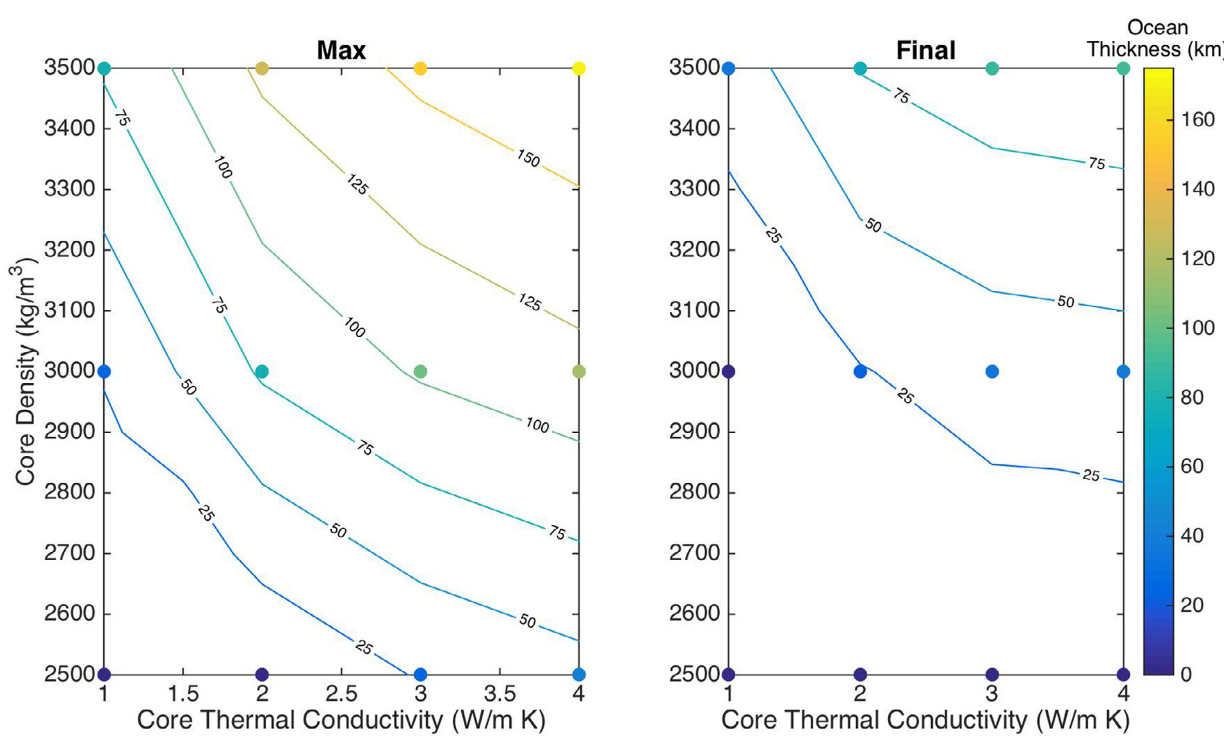

Fig. C1. Final and maximum ocean thickness for all model runs with $\phi_0 = 0.0$, $\rho_{ice} = 920$ kg/m^3, and no mass conservation. This figure is meant to be equivalent to Hammond et al. (2016) Figure S3 (0% ammonia).

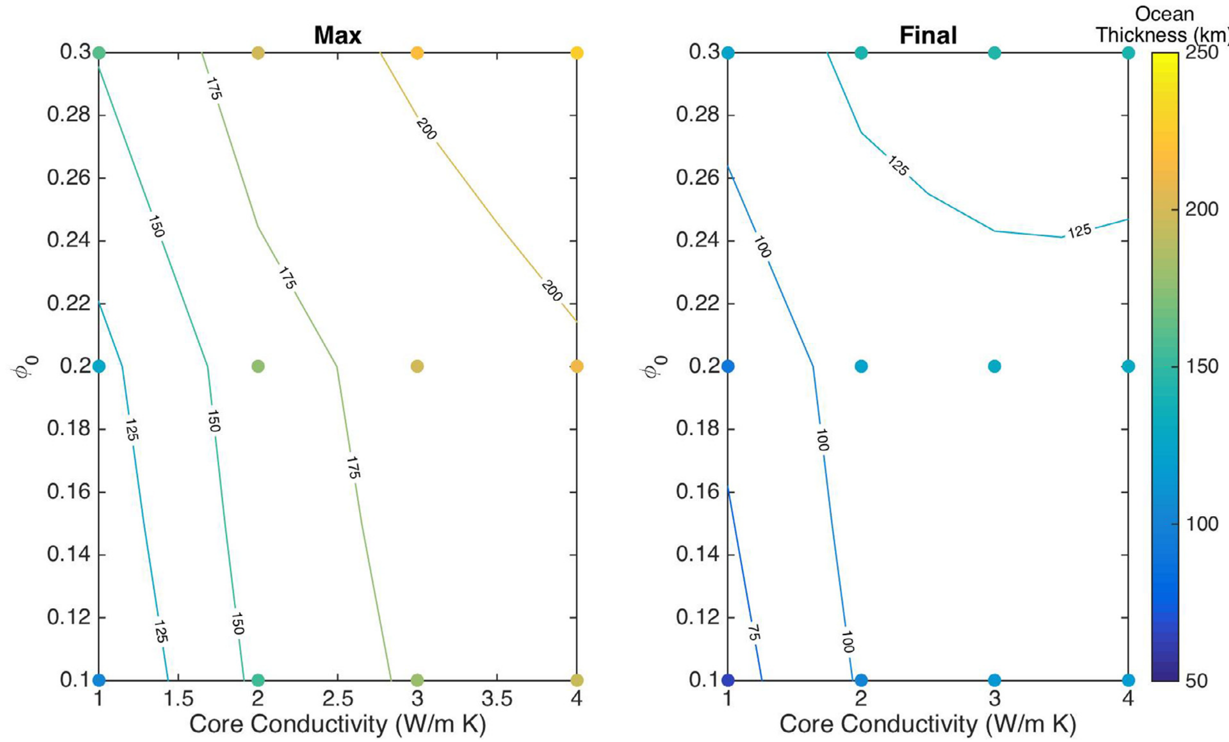

Fig. C2. Final and maximum ocean thickness for all model runs with $\rho_c = 3500$ kg/m^3, $\rho_{ice} = 950$ kg/m^3, $\eta_0 = 10^{14}$ Pa s (same as those plotted in Fig. 2.

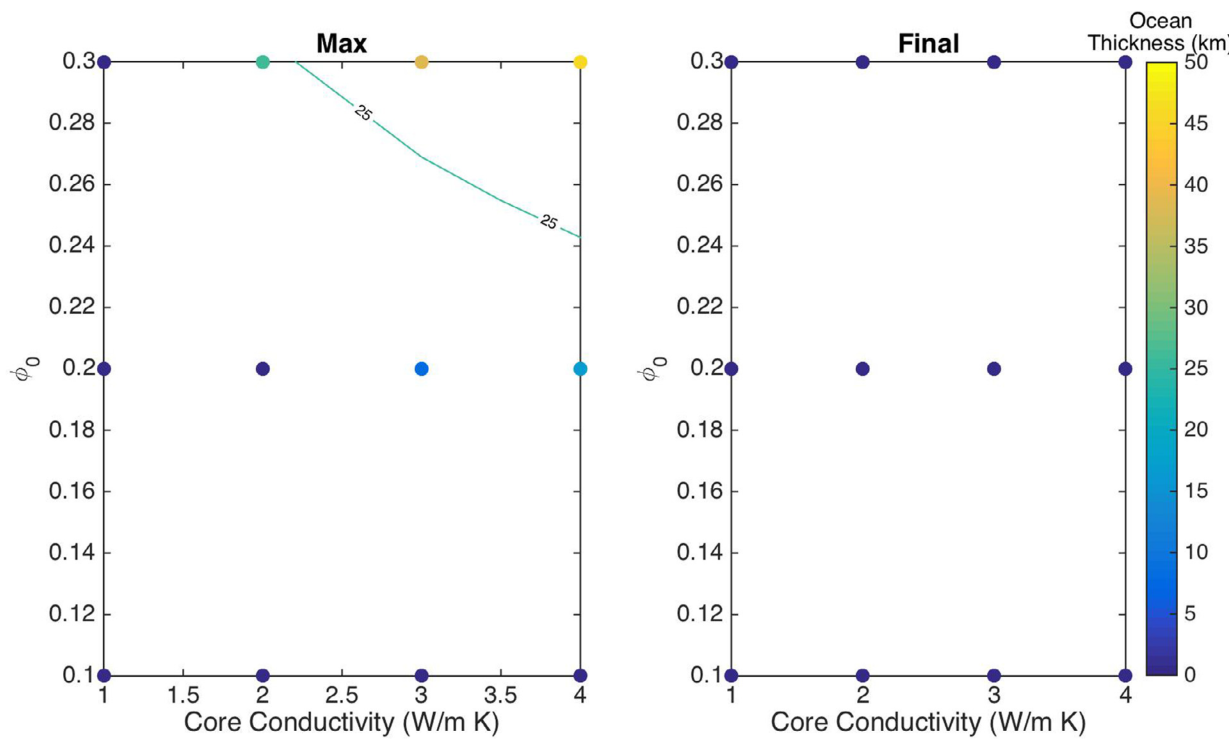

Fig. C3. Same as Fig. C.4 only for Charon.

Appendix D. Diffusion derivation

The thermal evolution of icy words is controlled by heat input via radioactive decay, and the ability of the body to transport that heat out of the core. The thermal evolution over time is primarily controlled by the equation for thermal diffusion on a sphere,

$$\frac{1}{\rho Cp}\frac{\partial T}{\partial t} = \frac{-1}{r^2}\frac{\partial}{\partial r}\left(-kr^2\frac{\partial T}{\partial r}\right) + H \qquad \text{(D.1)}$$

This equation can also be written in terms of the heat flux (F),

$$F = kr^2\frac{\partial T}{\partial r} \qquad \text{(D.2)}$$

$$\frac{1}{\rho Cp}\frac{\partial T}{\partial t} = \frac{1}{r^2}\frac{\partial F}{\partial r} + H \quad (D.3)$$

We discretize this equation as

$$\frac{1}{\rho_i Cp_i}\frac{\Delta T_i}{\Delta t} = \frac{1}{r_i^2}\frac{F_{i+1/2} - F_{i-1/2}}{\Delta z_i} + H \quad (D.4)$$

With this assumption in place, we can follow the method of Kieffer (2013) to solve for the heat flux at each layer boundary. The heat flux at the top of a layer is

$$F_{i+1/2} = \frac{T_{i+1/2} - T_i}{\Delta z_i/2} k_i r_{i+1/2}^2 \quad (D.5)$$

and at the bottom of the layer

$$F_{i-1/2} = \frac{T_i - T_{i+1/2}}{\Delta z_i/2} k_i r_{i-1/2}^2 \quad (D.6)$$

Because the temperature at the top of one layer must match the temperature at the bottom of the next, we can solve for the flux at this boundary and attain

$$F_{i+1/2} = 2r_{i+1/2}^2 \frac{T_{i+1} - T_i}{\frac{\Delta z_{i+1}}{k_{i+1}} + \frac{\Delta z_i}{k_i}} \quad (D.7)$$

and

$$F_{i+1/2} = 2r_{i+1/2}^2 \frac{T_{i+1} - T_i}{\frac{\Delta z_{i+1}}{k_{i+1}} + \frac{\Delta z_i}{k_i}} \quad (D.8)$$

Any layer where the temperature of the ice exceeds the melting temperature begins melting. It is assumed that layers with any amount of melt are fixed at the local melt temperature. Any net flux into or out of ocean layers causes melting or freezing. Because the ocean has this fixed temperature condition, Eq. (D.5) is modified such that the layer boundary temperature for the layer above and below the ocean is set to the adjacent ocean melt temperature. For the core ocean interface this is given by

$$F_{i+1/2} = r_{i+1/2}^2 k_i \frac{T_{melt,i-1} - T_i}{\Delta z_i/2} \quad (D.9)$$

Appendix E. Model results

Table E1
Summary of model runs. Δz_ϕ is the final porous layer thickness and F_c is the heat flux out of the core at the end of the model run. Results listed does include the effect of compression. Charon's ocean completely freezes in every model run.

Parameters			Pluto					Charon			$\Delta\rho_{PC}$
f_{rock}	k_c W/m K	η_0 Pa s	Final radius (km)	Max ocean (km)	Final ocean (km)	Δz_ϕ (km)	F_c (mW/m^2)	Final radius (km)	Max ocean (km)	Δz_ϕ (km)	kg/m^3
0.66	2.0	1.00E+13	1200.3	147.7	96.4	145.1	5.2	601.0	0.0	153.3	56.9
0.66	1.0	1.00E+14	1207.0	102.1	65.5	190.5	4.4	604.2	0.0	178.5	54.7
0.66	2.0	1.00E+14	1203.7	154.6	102.3	147.6	5.2	603.5	0.0	156.7	63.0
0.66	3.0	1.00E+14	1202.1	179.0	113.6	126.9	5.5	603.0	0.0	148.4	66.7
0.66	4.0	1.00E+14	1201.2	193.9	116.1	115.1	5.5	602.8	0.0	143.7	68.7
0.66	2.0	1.00E+17	1205.4	158.4	105.4	161.5	5.2	604.7	0.0	171.1	65.8
0.68	2.0	1.00E+13	1198.2	141.0	90.0	140.4	5.2	601.3	0.0	149.6	66.1
0.68	1.0	1.00E+14	1205.7	97.0	59.8	184.5	4.4	604.4	0.0	174.8	58.9
0.68	2.0	1.00E+14	1200.9	147.3	95.1	141.2	5.2	603.6	0.0	153.6	72.8
0.68	3.0	1.00E+14	1198.9	170.4	106.1	122.2	5.5	603.1	0.0	144.5	78.4
0.68	4.0	1.00E+14	1197.8	184.4	108.6	110.6	5.6	602.9	0.0	140.0	80.8
0.68	2.0	1.00E+17	1202.3	150.6	97.8	156.0	5.2	604.7	0.0	167.5	76.1
0.71	1.0	1.00E+14	1188.9	108.6	70.5	146.2	4.4	600.6	0.0	146.6	105.2
0.71	2.0	1.00E+14	1182.8	153.7	99.6	109.4	5.3	598.3	0.0	126.9	114.1
0.71	3.0	1.00E+14	1180.1	173.7	107.4	93.1	5.6	597.4	0.0	119.0	118.5
0.71	4.0	1.00E+14	1178.6	185.7	108.1	84.1	5.6	596.4	8.8	111.9	117.2
0.76	1.0	1.00E+14	1216.2	0.0	0.0	171.1	4.0	605.8	0.0	119.5	24.6
0.76	2.0	1.00E+14	1213.9	43.8	0.0	130.2	4.7	605.7	0.0	119.4	34.2
0.76	3.0	1.00E+14	1212.6	65.9	0.1	112.6	4.8	605.6	0.0	119.4	38.9
0.76	4.0	1.00E+14	1211.8	79.3	1.4	102.1	4.6	605.4	0.0	117.5	40.2
0.69	1.0	1.00E+14	1199.2	118.3	80.7	151.4	4.4	606.1	0.0	152.8	108.5
0.69	2.0	1.00E+14	1193.0	164.7	110.6	112.8	5.3	603.9	0.0	132.2	117.9
0.69	3.0	1.00E+14	1190.2	185.3	118.4	96.8	5.6	602.8	4.1	122.9	121.1
0.69	4.0	1.00E+14	1188.7	197.7	119.1	87.4	5.6	601.8	12.9	115.4	120.0
0.69	2.0	1.00E+13	1201.0	160.1	109.9	126.8	5.2	607.2	0.0	140.8	104.3
0.67	1.0	1.00E+14	1210.5	127.3	91.3	158.1	4.4	612.7	0.0	158.1	107.0
0.67	2.0	1.00E+14	1204.2	175.9	122.2	118.7	5.2	610.5	0.0	138.1	117.0
0.67	3.0	1.00E+14	1201.4	197.4	130.1	100.7	5.5	609.2	8.1	126.5	119.0
0.67	4.0	1.00E+14	1199.8	210.1	130.5	90.7	5.5	608.2	16.9	119.6	118.2
0.67	2.0	1.00E+17	1206.2	184.8	128.5	128.1	5.2	612.5	0.6	150.3	124.7
0.71	2.0	1.00E+13	1198.7	154.0	103.9	120.5	5.3	607.8	0.0	136.8	116.4
0.69	1.0	1.00E+14	1208.2	122.3	84.7	151.6	4.4	612.9	0.0	154.2	115.5
0.69	2.0	1.00E+14	1200.8	167.6	113.8	112.9	5.3	610.6	0.0	134.7	130.3
0.69	3.0	1.00E+14	1197.6	187.7	121.4	96.3	5.6	609.3	7.1	123.4	133.6
0.69	4.0	1.00E+14	1196.0	199.9	122.0	86.5	5.6	608.3	15.8	115.6	132.6
0.69	2.0	1.00E+17	1202.4	175.1	119.6	124.4	5.3	612.6	0.0	147.4	139.3
0.72	1.0	1.00E+14	1179.7	141.3	99.3	93.9	4.4	600.7	0.0	106.6	147.3
0.72	2.0	1.00E+14	1172.9	176.1	118.0	69.2	5.3	596.3	18.7	86.6	141.5
0.72	3.0	1.00E+14	1170.2	191.4	121.7	59.3	5.6	594.3	30.4	77.0	136.7
0.72	4.0	1.00E+14	1168.7	200.4	120.1	53.5	5.7	593.1	37.2	72.0	133.4
0.75	1.0	1.00E+14	1227.1	28.7	0.0	142.6	3.9	618.0	0.0	132.7	78.2
0.75	2.0	1.00E+14	1221.5	72.9	15.9	106.8	4.4	615.8	0.0	117.6	84.6

(continued on next page)

Table E1 (*continued*)

Parameters			Pluto					Charon			$\Delta\rho_{PC}$
f_{rock}	k_c W/m K	η_0 Pa s	Final radius (km)	Max ocean (km)	Final ocean (km)	Δz_ϕ (km)	F_c (mW/m^2)	Final radius (km)	Max ocean (km)	Δz_ϕ (km)	kg/m^3
0.75	3.0	1.00E+14	1218.9	92.4	22.8	91.5	4.6	614.7	0.0	108.8	86.5
0.75	4.0	1.00E+14	1217.4	103.9	22.5	82.5	4.6	614.0	0.0	103.7	87.3
0.70	1.0	1.00E+14	1189.9	151.4	110.4	97.4	4.4	605.9	0.0	110.8	145.8
0.70	2.0	1.00E+14	1182.9	187.4	129.4	72.6	5.3	601.3	22.4	88.9	139.4
0.70	3.0	1.00E+14	1180.0	203.4	132.9	61.1	5.6	599.3	34.4	79.7	135.0
0.70	4.0	1.00E+14	1178.5	212.7	131.1	55.1	5.6	598.1	41.1	74.5	132.0
0.69	1.0	1.00E+14	1201.0	162.0	122.8	102.6	4.4	612.2	0.0	114.6	143.1
0.69	2.0	1.00E+14	1193.7	199.8	142.1	75.3	5.3	607.3	26.4	92.4	136.3
0.69	3.0	1.00E+14	1190.7	216.3	145.5	64.3	5.6	605.2	38.5	82.7	132.4
0.69	4.0	1.00E+14	1189.1	226.0	143.4	58.0	5.6	604.0	45.3	77.4	129.7
0.69	2.0	1.00E+17	1195.3	211.9	150.8	81.9	5.3	609.2	37.9	100.1	145.0
0.71	1.0	1.00E+14	1197.4	155.9	114.5	98.6	4.4	612.3	0.0	112.9	163.2
0.71	2.0	1.00E+14	1189.6	190.8	132.9	71.7	5.3	607.3	25.5	90.0	158.6
0.71	3.0	1.00E+14	1186.5	206.1	136.3	60.9	5.6	605.2	37.4	80.4	154.9
0.71	4.0	1.00E+14	1185.0	215.2	134.4	54.6	5.6	604.0	44.0	75.1	151.6
0.71	2.0	1.00E+17	1190.8	201.9	141.0	79.4	5.3	609.2	36.7	97.6	168.1
0.76	1.0	1.00E+14	1225.7	67.5	22.1	93.1	3.7	620.1	0.0	100.1	105.4
0.76	2.0	1.00E+14	1219.1	102.0	40.5	69.1	4.4	616.5	0.0	84.3	105.1
0.76	3.0	1.00E+14	1216.4	116.9	43.4	59.0	4.6	615.0	0.0	77.9	104.8
0.76	4.0	1.00E+14	1214.9	125.9	40.8	52.9	4.6	614.2	0.0	74.4	104.5

References

Ahrens, T.J., Gaffney, E.S., 1971. Dynamic compression of enstatite. J. Geophys. Res. 76 (23), 5504–5513. doi:10.1029/JB076i023p05504.

Arakawa, M., Leliwa-Kopystynski, J., Maeno, N., 2002. Impact experiments on porous icy-silicate cylindrical blocks and the implication for disruption and accumulation of small icy bodies. Icarus 158 (2), 516–531. https://doi.org/10.1006/icar.2002.6893.

Baer, J., Chesley, S.R., Matson, R.D., 2011. Astrometric masses of 26 asteroids and observations on asteroid porosity. Astron. J. (N. Y.) 141 (5), 143.

Barr, A.C., Collins, G.C., 2015. Tectonic activity on Pluto after the Charon-forming impact. Icarus 246, 146–155. https://doi.org/10.1016/j.icarus.2014.03.042. Special Issue: The Pluto System.

Besserer, J., Nimmo, F., Roberts, J.H., Pappalardo, R.T., 2013. Convection-driven compaction as a possible origin of Enceladus's long wavelength topography. J. Geophys. Res.: Planets 118 (5), 908–915. Note that there is an error in equation 2b, 10.1002/jgre.20079.

Besserer, J., Nimmo, F., Wieczorek, M.A., Weber, R.C., Kiefer, W.S., McGovern, P.J., Andrews-Hanna, J.C., Smith, D.E., Zuber, M.T., 2014. GRAIL gravity constraints on the vertical and lateral density structure of the lunar crust. Geophys. Res. Lett. 41 (16), 5771–5777. doi:10.1002/2014GL060240.

Beyer, R.A., Nimmo, F., McKinnon, W.B., Moore, J.M., Binzel, R.P., Conrad, J.W., Cheng, A., Ennico, K., Lauer, T.R., Olkin, C., Robbins, S., Schenk, P., Singer, K., Spencer, J.R., Stern, S.A., Weaver, H., Young, L., Zangari, A.M., 2016. Charon tectonics. Icarus. https://doi.org/10.1016/j.icarus.2016.12.018.

Brown, M.E., 2012. The compositions of Kuiper belt objects. Annu. Rev. Earth Planet. Sci. 40 (1), 467–494. doi:10.1146/annurev-earth-042711-105352.

Brozović, M., Showalter, M.R., Jacobson, R.A., Buie, M.W., 2015. The orbits and masses of satellites of Pluto. Icarus 246, 317–329. https://doi.org/10.1016/j.icarus.2014.03.015. Special Issue: The Pluto System.

Buie, M.W., Cruikshank, D.P., Lebofsky, L.A., Tedesco, E.F., 1987. Water frost on Charon. Nature 329 (6139), 522–523.

Candela, P., Crummett, C., Earnest, D., Frank, M., Wylie, A., 2007. Low-pressure decomposition of chrysotile as a function of time and temperature. Am. Mineral. 92 (10), 1704–1713. doi:10.2138/am.2007.2559.

Canup, R.M., 2005. A giant impact origin of Pluto–Charon. Science 307 (5709), 546–550. doi:10.1126/science.1106818.

Canup, R.M., 2011. On a giant impact origin of Charon, Nix, and Hydra. Astron. J. (N. Y.) 141 (2), 35.

Castillo-Rogez, J., Matson, D., Sotin, C., Johnson, T., Lunine, J., Thomas, P., 2007. Iapetus' geophysics: Rotation rate, shape, and equatorial ridge. Icarus 190 (1), 179–202. https://doi.org/10.1016/j.icarus.2007.02.018.

Cheng, W., Lee, M.H., Peale, S., 2014. Complete tidal evolution of Pluto–Charon. Icarus 233, 242–258. https://doi.org/10.1016/j.icarus.2014.01.046.

Consolmagno, G., Britt, D., Macke, R., 2008. The significance of meteorite density and porosity. Chemie der Erde - Geochemistry 68 (1), 1–29. https://doi.org/10.1016/j.chemer.2008.01.003.

Crovisier, J., 1994. Molecular abundances in comets. In: Symposium - International Astronomical Union, 160, p. 313326. doi:10.1017/S0074180900046611.

Cruikshank, D., Grundy, W., DeMeo, F., Buie, M., Binzel, R., Jennings, D., Olkin, C., Parker, J., Reuter, D., Spencer, J., Stern, S., Young, L., Weaver, H., 2015. The surface compositions of Pluto and Charon. Icarus 246, 82–92. Special Issue: The Pluto System, https://doi.org/10.1016/j.icarus.2014.05.023.

Desch, S., Neveu, M., 2016. Differentiation and cryovolcanism on Charon: a view before and after new horizons. Icarus. https://doi.org/10.1016/j.icarus.2016.11.037.

Desch, S.J., 2015. Density of Charon formed from a disk generated by the impact of partially differentiated bodies. Icarus 246, 37–47. Special Issue: The Pluto System, https://doi.org/10.1016/j.icarus.2014.07.034.

Dlugogorski, B.Z., Balucan, R.D., 2014. Dehydroxylation of serpentine minerals: implications for mineral carbonation. Renewable Sustainable Energy Rev. 31, 353–367. doi:10.1016/j.rser.2013.11.002.

Durham, W., Prieto-Ballesteros, O., Goldsby, D., Kargel, J., 2010. Rheological and thermal properties of icy materials. Space Sci. Rev. 153 (1–4), 273–298.

Eberhardt, P., Krankowsky, D., Schulte, W., Dolder, U., Lämmerzahl, P., Berthelier, J.J., Woweries, J., Stubbemann, U., Hodges, R.R., Hoffman, J.H., Illiano, J.M., 1988. The CO and N2 abundance in comet P/Halley. Springer Berlin Heidelberg, Berlin, Heidelberg, pp. 481–484. doi:10.1007/978-3-642-82971-0_87.

Eluszkiewicz, J., 1990. Compaction and internal structure of Mimas. Icarus 84 (1), 215–225. https://doi.org/10.1016/0019-1035(90)90167-8.

Eluszkiewicz, J., 2004. Dim prospects for radar detection of Europa's ocean. Icarus 170 (1), 234–236. https://doi.org/10.1016/j.icarus.2004.02.011.

Fowler, A.C., 1985. A mathematical model of magma transport in the asthenosphere. Geophys. Astrophys. Fluid Dyn. 33 (1–4), 63–96. doi:10.1080/03091928508245423.

Goldblatt, C., Robinson, T.D., Zahnle, K.J., Crisp, D., 2013. Low simulated radiation limit for runaway greenhouse climates. Nat. Geosci. 6 (8), 661–667.

Graham, E.K., Barsch, G.R., 1969. Elastic constants of single-crystal forsterite as a function of temperature and pressure. J. Geophys. Res. 74 (25), 5949–5960. doi:10.1029/JB074i025p05949.

Grundy, W.M., Binzel, R.P., Buratti, B.J., Cook, J.C., Cruikshank, D.P., Dalle Ore, C.M., Earle, A.M., Ennico, K., Howett, C.J.A., Lunsford, A.W., Olkin, C.B., Parker, A.H., Philippe, S., Protopapa, S., Quirico, E., Reuter, D.C., Schmitt, B., Singer, K.N., Verbiscer, A.J., Beyer, R.A., Buie, M.W., Cheng, A.F., Jennings, D.E., Linscott, I.R., Parker, J.W., Schenk, P.M., Spencer, J.R., Stansberry, J.A., Stern, S.A., Throop, H.B., Tsang, C.C.C., Weaver, H.A., Weigle, G.E., Young, L.A., science team, T.N.H., 2016. Surface compositions across Pluto and Charon. Science 351 (6279). doi:10.1126/science.aad9189.

Hammond, N.P., Barr, A.C., Parmentier, E.M., 2016. Recent tectonic activity on Pluto driven by phase changes in the ice shell. Geophys. Res. Lett. n/a–n/a. 2016GL069220 10.1002/2016GL069220.

Hobbs, P.V., 1974. Ice physics. Oxford University Press.

Hunten, D.M., Watson, A.J., 1982. Stability of Pluto's atmosphere. Icarus 51 (3), 665–667. https://doi.org/10.1016/0019-1035(82)90155-5.

Inoue, T., Yoshimi, I., Yamada, A., Kikegawa, T., 2009. Time-resolved x-ray diffraction analysis of the experimental dehydration of serpentine at high pressure. J. Mineral. Petrol. Sci. 104 (2), 105–109. doi:10.2465/jmps.081022d.

Irene, E.A., Tierney, E., Angilello, J., 1982. A viscous flow model to explain the appearance of high density thermal Sio2 at low oxidation temperatures. J. Electrochem. Soc. 129 (11), 2594–2597. doi:10.1149/1.2123617.

Jiang, F., Speziale, S., Duffy, T.S., 2006. Single-crystal elasticity of brucite, mg (oh) 2, to 15 gpa by brillouin scattering. Am. Mineral. 91 (11–12), 1893–1900.

Jiang, G.J., Person, W.B., Brown, K.G., 1975. Absolute infrared intensities and band shapes in pure solid co and co in some solid matrices. J. Chem. Phys. 62 (4), 1201–1211. https://doi.org/10.1063/1.430634.

Johansen, A., Low, M.-M.M., Lacerda, P., Bizzarro, M., 2015. Growth of asteroids, planetary embryos, and Kuiper belt objects by chondrule accretion. Sci. Adv. 1 (3). doi:10.1126/sciadv.1500109.

Kenyon, S.J., 2002. Planet formation in the outer solar system. Publ. Astron. Soc. Pac. 114 (793), 265.

Kenyon, S.J., Bromley, B.C., O'Brien, D.P., Davis, D.R., 2008. Formation and collisional evolution of Kuiper belt objects. Solar Syst. Beyond Neptune 293.

Kenyon, S.J., Luu, J.X., 1999. Accretion in the early Kuiper belt. ii. fragmentation. Astron. J. (N. Y.) 118 (2), 1101.
Kieffer, H., 2013. Thermal model for analysis of mars infrared mapping. J. Geophys. Res.: Planets 118 (3), 451–470. doi:10.1029/2012JE004164.
Leliwa-Kopystyński, J., Maruyama, M., Nakajima, T., 2002. The water-ammonia phase diagram up to 300 mpa: application to icy satellites. Icarus 159 (2), 518–528. https://doi.org/10.1006/icar.2002.6932.
Lellouch, E., Sicardy, B., de Bergh, C., Käufl, H.-U., Kassi, S., Campargue, A., 2009. Pluto'S lower atmosphere structure and methane abundance from high-resolution spectroscopy and stellar occultations. A&A 495 (3), L17–L21. doi:10.1051/0004-6361/200911633.
Malamud, U., Perets, H.B., Schubert, G., 2016. The contraction/expansion history of Charon with implication for its planetary scale tectonic belt. ArXiv e-prints. 1603.00875.
Malamud, U., Prialnik, D., 2015. Modeling Kuiper belt objects Charon, Orcus and Salacia by means of a new equation of state for porous icy bodies. Icarus 246, 21–36.
Malamud, U., Prialnik, D., 2016. A 1-d evolutionary model for icy satellites, applied to Enceladus. Icarus 268, 1–11. https://doi.org/10.1016/j.icarus.2015.12.046.
Marcialis, R.L., Rieke, G.H., Lebofsky, L.A., 1987. The surface composition of charon? Tentative identification of water ice. Science 237. 1349–51
McKinnon, W.B., Stern, S., Weaver, H., Nimmo, F., Bierson, C., Cook, J., Grundy, W., Cruikshank, D., Parker, A., Moore, J., Spencer, J., Young, L., Olkin, C., Smith, K.E., 2017. Origin of the Pluto–Charon system: constraints from the new horizons flyby. Icarus. https://doi.org/10.1016/j.icarus.2016.11.019.
Milbury, C., Johnson, B.C., Melosh, H.J., Collins, G.S., Blair, D.M., Soderblom, J.M., Nimmo, F., Bierson, C.J., Phillips, R.J., Zuber, M.T., 2015. Pre-impact porosity controls the gravity signature of lunar craters. Geophys. Res. Lett. 42 (17). doi:10.1002/2015GL066198.
Moore, J.M., McKinnon, W.B., Spencer, J.R., Howard, A.D., Schenk, P.M., Beyer, R.A., Nimmo, F., Singer, K.N., Umurhan, O.M., White, O.L., Stern, S.A., Ennico, K., Olkin, C.B., Weaver, H.A., Young, L.A., Binzel, R.P., Buie, M.W., Buratti, B.J., Cheng, A.F., Cruikshank, D.P., Grundy, W.M., Linscott, I.R., Reitsema, H.J., Reuter, D.C., Showalter, M.R., Bray, V.J., Chavez, C.L., Howett, C.J.A., Lauer, T.R., Lisse, C.M., Parker, A.H., Porter, S.B., Robbins, S.J., Runyon, K., Stryk, T., Throop, H.B., Tsang, C.C.C., Verbiscer, A.J., Zangari, A.M., Chaikin, A.L., Wilhelms, D.E., Team, N.H.S., 2016. The geology of Pluto and Charon through the eyes of new horizons. Science 351 (6279), 1284–1293. doi:10.1126/science.aad7055.
Mumma, M.J., Charnley, S.B., 2011. The chemical composition of comets-emerging taxonomies and natal heritage. Annu. Rev. Astron. Astrophys. 49 (1), 471–524. doi:10.1146/annurev-astro-081309-130811.
Nesvorný, D., Youdin, A.N., Richardson, D.C., 2010. Formation of Kuiper belt binaries by gravitational collapse. Astron. J. (N. Y.) 140 (3), 785.
Nimmo, F., Hamilton, D.P., McKinnon, W.B., Schenk, P.M., Binzel, R.P., Bierson, C.J., Beyer, R.A., Moore, J.M., Stern, S.A., Weaver, H.A., Olkin, C.B., Young, L.A., Smith, K.E., New Horizons Geology, G..I.T.T., 2016. Reorientation of Sputnik Planitia implies a subsurface ocean on Pluto. Nature. advance online publication
Nimmo, F., Pappalardo, R., Giese, B., 2003. On the origins of band topography, Europa. Icarus 166 (1), 21–32. https://doi.org/10.1016/j.icarus.2003.08.002.
Nimmo, F., Spencer, J., 2014. Powering Triton recent geological activity by obliquity tides: implications for Pluto geology. Icarus 1–9. doi:10.1016/j.icarus.2014.01.044.
Nimmo, F., Umurhan, O.M., Lisse, C.M., Bierson, C.J., Lauer, T.R., Buie, M.W., Throop, H.B., Kammer, J.A., Roberts, J.H., McKinnon, W.B., Moore, J.M., Stern, S., Young, L.A., Weaver, H.A., Olkin, C.B., Ennico, K., 2016. The new horizons GGI team mean radius and shape of Pluto and Charon from new horizons images. ArXiv e-prints. 1603.00821.
Petrenko, V.F., Whitworth, R.W., 2002. Elastic, thermal, and lattice dynamical properties. Physics of Ice. Oxford University Press, Oxford.
Protopapa, S., Boehnhardt, H., Herbst, T.M., Cruikshank, D.P., Grundy, W.M., Merlin, F., Olkin, C.B., 2008. Surface characterization of Pluto and Charon by l and m band spectra. A&A 490 (1), 365–375. doi:10.1051/0004-6361:200809994.
Pundsack, F.L., 1956. The properties of asbestos. II. The density and structure of chrysotile. J. Phys. Chem. 60 (3), 361–364. doi:10.1021/j150537a027.
Robuchon, G., Nimmo, F., 2011. Thermal evolution of Pluto and implications for surface tectonics and a subsurface ocean. Icarus 216 (2), 426–439. https://doi.org/10.1016/j.icarus.2011.08.015.
Sawai, M., Katayama, I., Hamada, A., Maeda, M., Nakashima, S., 2013. Dehydration kinetics of antigorite using in situ high-temperature infrared microspectroscopy. Phys. Chem. Miner. 40 (4), 319–330. doi:10.1007/s00269-013-0573-9.
Schaller, E.L., Brown, M.E., 2007. Volatile loss and retention on Kuiper belt objects. Astrophys. J. Lett. 659 (1), L61.
Shoshany, Y., Prialnik, D., Podolak, M., 2002. Monte Carlo modeling of the thermal conductivity of porous cometary ice. Icarus 157 (1), 219–227. https://doi.org/10.1006/icar.2002.6815.
Stern, S.A., Bagenal, F., Ennico, K., Gladstone, G.R., Grundy, W.M., McKinnon, W.B., Moore, J.M., Olkin, C.B., Spencer, J.R., Weaver, H.A., Young, L.A., Andert, T., Andrews, J., Banks, M., Bauer, B., Bauman, J., Barnouin, O.S., Bedini, P., Beisser, K., Beyer, R.A., Bhaskaran, S., Binzel, R.P., Birath, E., Bird, M., Bogan, D.J., Bowman, A., Bray, V.J., Brozovic, M., Bryan, C., Buckley, M.R., Buie, M.W., Buratti, B.J., Bushman, S.S., Calloway, A., Carcich, B., Cheng, A.F., Conard, S., Conrad, C.A., Cook, J.C., Cruikshank, D.P., Custodio, O.S., Dalle Ore, C.M., Deboy, C., Dischner, Z.J.B., Dumont, P., Earle, A.M., Elliott, H.A., Ercol, J., Ernst, C.M., Finley, T., Flanigan, S.H., Fountain, G., Freeze, M.J., Greathouse, T., Green, J.L., Guo, Y., Hahn, M., Hamilton, D.P., Hamilton, S.A., Hanley, J., Harch, A., Hart, H.M., Hersman, C.B., Hill, A., Hill, M.E., Hinson, D.P., Holdridge, M.E., Horanyi, M., Howard, A.D., Howett, C.J.A., Jackman, C., Jacobson, R.A., Jennings, D.E., Kammer, J.A., Kang, H.K., Kaufmann, D.E., Kollmann, P., Krimigis, S.M., Kusnierkiewicz, D., Lauer, T.R., Lee, J.E., Lindstrom, K.L., Linscott, I.R., Lisse, C.M., Lunsford, A.W., Mallder, V.A., Martin, N., McComas, D.J., McNutt, R.L., Mehoke, D., Mehoke, T., Melin, E.D., Mutchler, M., Nelson, D., Nimmo, F., Nunez, J.I., Ocampo, A., Owen, W.M., Paetzold, M., Page, B., Parker, A.H., Parker, J.W., Pelletier, F., Peterson, J., Pinkine, N., Piquette, M., Porter, S.B., Protopapa, S., Redfern, J., Reitsema, H.J., Reuter, D.C., Roberts, J.H., Robbins, S.J., Rogers, G., Rose, D., Runyon, K., Retherford, K.D., Ryschkewitsch, M.G., Schenk, P., Schindhelm, E., Sepan, B., Showalter, M.R., Singer, K.N., Soluri, M., Stanbridge, D., Steffl, A.J., Strobel, D.F., Stryk, T., Summers, M.E., Szalay, J.R., Tapley, M., Taylor, A., Taylor, H., Throop, H.B., Tsang, C.C.C., Tyler, G.L., Umurhan, O.M., Verbiscer, A.J., Versteeg, M.H., Vincent, M., Webbert, R., Weidner, S., Weigle, G.E., White, O.L., Whittenburg, K., Williams, B.G., Williams, K., Williams, S., Woods, W.W., Zangari, A.M., Zirnstein, E., 2015. The Pluto system: initial results from its exploration by new horizons. Science 350 (6258). doi:10.1126/science.aad1815.
Tholen, D.J., Buie, M.W., 1997. Bulk properties of Pluto and Charon. Pluto Charon 1, 193.
Thomas, P.C., Armstrong, J.W., Asmar, S.W., Burns, J.A., Denk, T., Giese, B., Helfenstein, P., Iess, L., Johnson, T.V., McEwen, A., Nicolaisen, L., Porco, C., Rappaport, N., Richardson, J., Somenzi, L., Tortora, P., Turtle, E.P., Veverka, J., 2007. Hyperionś sponge-like appearance. Nature 448 (7149), 50–56.
Tian, F., Toon, O.B., 2005. Hydrodynamic escape of nitrogen from Pluto. Geophys. Res. Lett. 32 (18), n/a–n/a. doi:10.1029/2005GL023510. L18201.
Tian, F., Toon, O.B., Pavlov, A.A., Sterck, H.D., 2005. Transonic hydrodynamic escape of hydrogen from extrasolar planetary atmospheres. Astrophys. J. 621 (2), 1049.
Trafton, L., 1980. Does Pluto have a substantial atmosphere? Icarus 44 (1), 53–61. https://doi.org/10.1016/0019-1035(80)90054-8.
Turcotte, D.L., Schubert, G., 2014. Geodynamics. Cambridge University Press.
Vance, S.D., Hand, K.P., Pappalardo, R.T., 2016. Geophysical controls of chemical disequilibria in Europa. Geophys. Res. Lett. 43 (10), 4871–4879. 2016GL068547 https://doi.org/10.1002/2016GL068547.
Wegner, W.W., Ernst, W., 1983. Experimentally determined hydration and dehydration reaction rates in the system Mgo-Sio2-H2O. Am. J. Sci. 283, 151–180.
Wieczorek, M.a., Neumann, G.a., Nimmo, F., Kiefer, W.S., Taylor, G.J., Melosh, H.J., Phillips, R.J., Solomon, S.C., Andrews-Hanna, J.C., Asmar, S.W., Konopliv, A.S., Lemoine, F.G., Smith, D.E., Watkins, M.M., Williams, J.G., Zuber, M.T., 2013. The crust of the moon as seen by GRAIL. Science (New York, N.Y.) 339 (6120). 671–5 10.1126/science.1231530.
Yasui, M., Arakawa, M., 2009. Compaction experiments on ice-silica particle mixtures: implication for residual porosity of small icy bodies. J. Geophys. Res.: Planets 114 (E9). E09004 10.1029/2009JE003374.